Aerospace Science and Technology 136 (2023) 108208

Contents lists available at ScienceDirect

Aerospace Science and Technology

journal homepage: www.elsevier.com/locate/aescte

Neural network-based multi-point, multi-objective optimisation for transonic applications

Fernando Tejero [a,*], David G. MacManus [a], Francisco Sanchez-Moreno [a], Christopher Sheaf [b]

[a] Centre for Propulsion Engineering, School of Aerospace, Transport and Manufacturing, Cranfield University, Bedfordshire, MK43 0AL, United Kingdom
[b] Rolls-Royce plc., P.O. box 31, Derby, DE24 8BJ, United Kingdom

ARTICLE INFO

Article history:
Received 11 October 2022
Received in revised form 27 January 2023
Accepted 18 February 2023
Available online 24 February 2023
Communicated by Z. Weiwei

Keywords:
Machine learning
Neural network
Nacelle
Aero-engine
Optimisation
Inverse design

ABSTRACT

In the context of aircraft applications, the overall design process can be challenging due to the different aerodynamic requirements at several operating conditions and the total associated computational overhead. For this reason, the use of low order models for the optimisation of complex non-linear problems is sometimes used. This paper addresses the challenge of transonic aerodynamic design optimisation through the integration of a set of neural networks for the prediction of integral values, the classification of flow features and the estimation of flow field characteristics. The design method improves the computational efficiency relative to an expensive design process driven by Computational Fluid Dynamics (CFD) evaluations. The approach is used for the multi-point, multi-objective optimisation of a compact aero-engine nacelle in which the design outcomes are validated using a CFD in-the-loop optimisation strategy. It is demonstrated that the method based on the neural network capability identifies similar nacelle designs at a 75% reduction in the overall computational cost, a drag uncertainty prediction within 2.8%, and a predictive accuracy for the classification metric of 98%. For downselected configurations, the main flow characteristics in terms of peak Mach number, pre-shock Mach number and shock location are well predicted by the neural network models compared with the CFD-based evaluations.

1. Introduction

For many aerospace applications, the design and optimisation of aerodynamic components is complex due to the large number of design variables, the non-linearity of transonic flow aerodynamics and the considerable cost of the overall process [1]. Different strategies have been developed to overcome these challenges. They include adjoint methods [2], surrogate models [3], hybrid routines that combine lower- and higher-fidelity evaluations [4] and feature-extraction approaches based on dimensionality reduction techniques [5]. Over the last years the advances in high-performance computing architectures have enabled the generation of large amounts of data. For this reason, machine learning within fluid mechanics has been used recently for different applications [6]. Ji et al. [7] carried out a comprehensive literature review of machine learning methods for aerodynamic shape optimisation. In particular, neural networks have been employed for a wide range of aerodynamic studies to drive the design process [8–10]. Secco et al. [11] investigated the application of artificial neural networks (ANN) for the prediction of lift and drag coefficients in wing-fuselage configurations. Overall, the model was built with 40 input variables, in which three were related to the operating condition (altitude, Mach number and angle of attack) and the rest were geometry parameters to define the wing shape. The aerodynamic database was generated with a full-potential code. For an independent database, the method had an average absolute error of 0.004 for the lift coefficient and 5 airframe drag counts. Lopez et al. [9] combined artificial neural networks and a dimensionality reduction capability based on the active subspace method for the optimisation of a transonic compressor fan blade. The ANNs were used to estimate the gradients across the design space and identify the active design subspaces (ADS). Through an iterative process in which the converge of the eigenvectors was monitored, a final ANN was built in the reduced space. It was demonstrated that this approach improves the accuracy in the predictions. For example, the coefficient of determination R^2 for the compressor efficiency was increased from 0.89 to 0.94 when the ANNs were trained in the original high-dimensional space and in the

* Corresponding author.
E-mail address: f.tejero@cranfield.ac.uk (F. Tejero).

https://doi.org/10.1016/j.ast.2023.108208

Nomenclature

Roman Symbols

A	Area
C_D	Nacelle drag
C_P	Pressure Distribution
D	Drag
f	Non-dimensional factor
L	Length
M	Mach Number

Greek Symbols

β	Boat-tail angle
ϕ	Force
ρ	Density

Superscripts and Subscripts

∞	Freestream
EoC	End of cruise
hi	Highlight
if	Initial Forebody
iM	Increased Mach number
max	Maximum radius
nac	Nacelle
post	Post-exit
pre	Pre-entry
te	Trailing Edge

Acronyms

ANN	Artificial Neural Network
CFD	Computational Fluid Dynamics
CST	Class Shape Transformation
DSE	Design Space Exploration
GCI	Grid Convergence Index
LHS	Latin Hypercube Sampling
MFCR	Mass Flow Capture Ratio
MOO	Multi-objective optimisation
NN	Neural Network
RANS	Reynolds Averaged Navier Stokes
RSM	Response Surface Model

reduced dimensional space, respectively. The developed method was used for optimisation studies, and relative to a state-of-the-art adjoint-based process, the developed capability yielded a design with similar aerodynamic performance and a reduction in the computational cost of 35%. The same data-driven method was also successfully employed to investigate the effect of tip leakage axial momentum flux on the efficiency and stability range of an axial fan [12]. Bouhlel et al. [13] developed a framework for aerofoil design and optimisation at subsonic and transonic flow regimes with ANNs. The tool used 14 design variables to define the aerofoil shape and the data was obtained with RANS CFD. During the training process, the gradient information across the design space was used to enhance the prediction accuracy of the aerodynamic coefficients. The developed surrogate model was used within an optimisation design process in which the derived aerofoils were compared with the shapes obtained from expensive CFD-based optimisations. For example, for a transonic case with M = 0.72 at fixed lift of C_L = 0.82, both design methods identified a similar aerofoil shape with a difference of 0.1 drag counts. Neural networks (NN) have been also used for flow feature identification and classification. Bosson and Nikoleris [14] investigated supervised learning techniques for aircraft trajectory applications. A range of machine learning algorithms were considered and it was found that the best classification accuracy was achieved with a multilayer perceptron (MLP) feed-forward ANN. The process yielded a NN model with a predictive accuracy of approximately 97%. Within the context of aerodynamic design, another key aspect is the capability to predict flow characteristics in terms of scalar and vector fields of the targeted aerodynamic design shape. This is pertinent when the process is closely linked with other disciplines in a multidisciplinary design environment [15,16]. For example, Bhatnagar et al. [17] developed a method to carry out flow-field predictions around aerofoils using convolutional NNs. The approach resulted in pressure and velocity estimations with a mean square error lower than 10% and a computational cost reduction of 4 orders of magnitude relative to RANS calculations. Zuo et al. [18] developed a multi-head perceptron neural network architecture to predict incompressible flow-fields around aerofoils. A convolutional neural network was used for the aerofoil parameterisation and, in combination with the aerodynamic inputs of Reynolds number and angle of attack, a multi-head perceptron was trained for the prediction of the velocity and pressure field. For an independent dataset, the proposed architecture resulted in flow-field predictions with a mean square error of approximately 10^{-5}, 10^{-6} and 10^{-7} for the X-velocity, Y-velocity and pressure, respectively. Sabater et al. [8] trained a multi-layer perceptron for transonic flow-field prediction. The method was successfully used to predict the flow around the NLR7301 profile, in which as input variables the angle of attacked varied from -3° and +5° and the Mach number ranged from 0.3 and 0.75. This approach was extended to the NASA Common Research model in which the Mach number changed from 0.5 to 0.88 and the MLP was used to predict the pressure distribution along the wing. It was demonstrated that the method was suitable for the prediction of shock-wave location and its intensity. Neural networks have been also successfully used in inverse design processes that aim to derive an aerodynamic shape that fulfils the user-prescribed targeted flow physics. Rai and Madavan [19] proposed a design strategy called parameter-based partitioning of the design space in which neural networks and polynomial fits were used. The process was successfully demonstrated in the redesign of a turbine aerofoil from a modern jet engine. Sun et al. [20] developed an inverse aerodynamic design method for transonic aerofoils and wings in which the shapes were described with 11 and 78 variables, respectively. The approach was used to identify geometries that fulfil specified aerodynamic requirements in terms of targeted lift, drag and momentum coefficients. A database was generated and different ANNs were built to predict the integral values. It was demonstrated that the approach yielded an aerofoil and wing shape definition with an aerodynamic performance within 2.5% of the targeted metrics. Kharal and Saleem [21] employed neural networks to predict an aerofoil geometry from a prescribed pressure distribution (C_p). The aerofoil was defined with 15 design variables and the Bezier-PARSEC parameterisation [22]. The method was applied for an incompressible flow regime and the database was generated with a panel method. It was concluded that a feed-forward backpropagation NN identified aerofoil geometries that met the user-prescribed C_p distributions. Neural networks have been also used for multidisciplinary studies that encompassed fluid-structure interaction investigations [23] or for aero-acoustic predictions [24]. Other studies have studied the efficacy of machine learning for calibrating turbulence models [25,26].

These previous studies using neural networks methods highlighted their suitability for a variety of aerodynamic design prob-

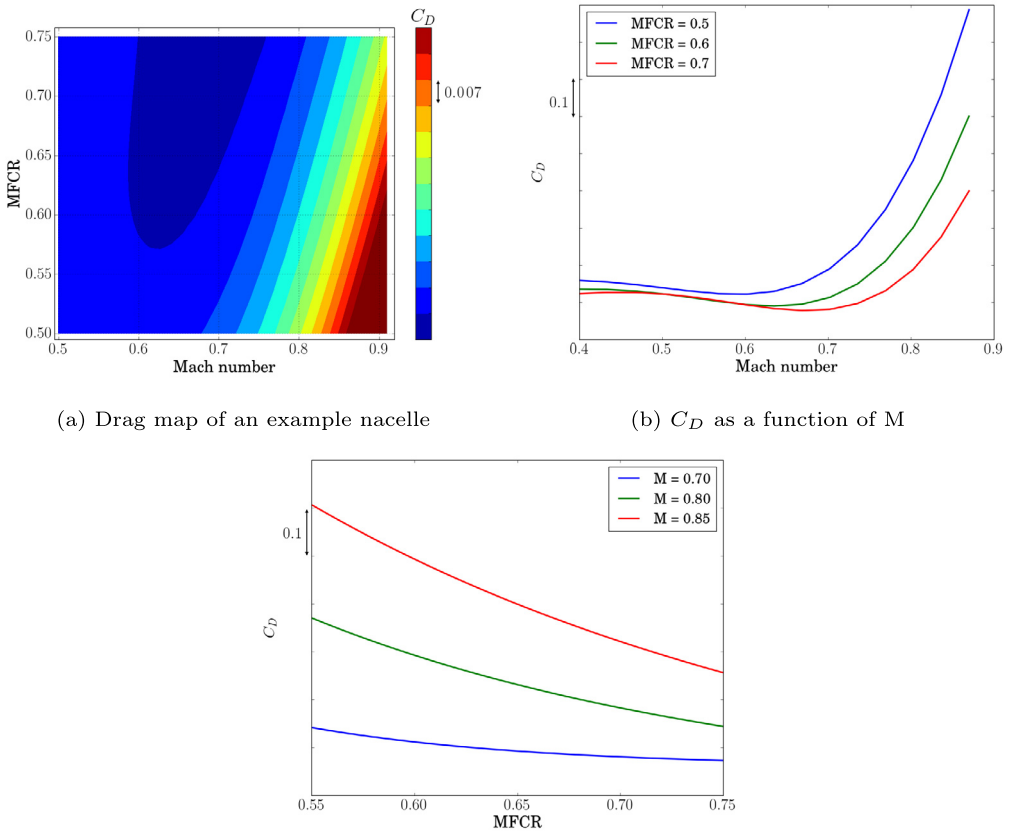

(a) Drag map of an example nacelle

(b) C_D as a function of M

(c) C_D as a function of MFCR

Fig. 1. Non-linearity of nacelle aerodynamics for key variables of Mach number (M) and massflow capture ratio (MFCR).

lems. Although the focus of this work is on the broader development and integration of different neural network architectures in a comprehensive design process, the test application is the design of a nacelle for a modern ultra high-bypass-ratio aero-engine. Future civil aero-engines are expected to operate with larger bypass ratios than current in-service architectures [27]. The aim is to reduce the specific thrust, improve the overall propulsive efficiency and, therefore, reduce the engine specific fuel consumption [28]. These new engine configurations may have larger fan diameters, which poses several challenges in the design process. If traditional design rules are used and the engines are accordingly scaled, the overall nacelle drag, weight, and effects of aircraft integration will increase [29]. For this reason, it is expected that the next generation of civil turbofan engines will have compact nacelles to meet the expected benefits from the new engine cycles [30,31]. The design and optimisation of compact aero-engine nacelles is a challenging problem due to the non-linearity associated with transonic aerodynamics and the wide range of operating conditions that are encountered throughout the flight envelope. For example, Fig. 1 shows the nacelle drag sensitivity to the two key operating conditions of Mach number (M) and massflow capture ratio (MFCR) for a compact aero-engine nacelle [32]. For a fixed flight Mach number, the nacelle drag coefficient (C_D) increases as the massflow capture ratio reduces caused by the flow acceleration around the nacelle lip. For a constant MFCR, C_D sharply increases at high M because of the compressibility effects and strong shock waves that manifest at those flight regimes. Due to the large changes on nacelle drag across different operating conditions, this aerodynamic design problem is typically addressed with a multi-point, multi-objective strategy to ensure aerodynamic robustness [32].

Previous nacelle design and optimisation studies have considered methods based on CFD in-the-loop or low order modelling. Tejero et al. [32] developed a framework for the optimisation of 2D axisymmetric compact aero-engine nacelles. Several multi-point, multi-objective optimisations (MOO) were carried out for a range of different normalised nacelle length (L_{nac}/r_{hi}) and trailing edge radius (r_{te}/r_{hi}). The process only considered operating conditions within the cruise segment in which the drag was minimised. Across the design space investigated, the mid-cruise nacelle drag varied by approximately 40%. The method was subsequently extended to accommodate a design and optimisation capability for 3D non-axisymmetric nacelle configurations [33]. It was used to quantify the impact of the intake droop and scarf angles on the nacelle drag characteristics of a compact aero-engine nacelle with L_{nac}/r_{hi} = 3.1 and r_{te}/r_{hi} = 0.91. The optimisation process was also based on cruise-type flight conditions. Different intake droop and scarf angles were considered and an independent CFD in-the-loop 3D MOO was carried for each configuration. Across the range of angles the mid-cruise nacelle drag changed by 3.5%. Schreiner et al. [34] carried out several optimisations for a range of 2D axisymmetric aero-engine nacelles in which L_{nac}/r_{hi} varied from 4.3 to 2.5. The process included flight conditions of the cruise segment as well as off-design windmilling scenarios [35]. It was found that compact nacelle architectures are more sensitive to windmilling. For example, a nacelle length reduction of L_{nac}/r_{hi} from 4.3 to 3.1 results in a mid-cruise drag benefit of around 15% if the downselection is based on cruise-type conditions. However, this erodes to 10.4% once windmilling considerations are taken into account. Silva et al. [36] developed a multi-point aerodynamic design method for ultra high-bypass-ratio turbofan engines. The design strategy considered critical operating conditions such as mid-cruise, low speed

at high angle of attack and crosswind. The process was not based on a optimisation process but in a manual design strategy. Relative to a baseline geometry with inlet separation at crosswind conditions, the redesign of the intake and external cowl to achieve fully-attached flow resulted in a 5.1% penalty at mid-cruise conditions.

Whilst the majority of nacelle studies in the open literature are based on numerical simulations, there are very limited investigations of surrogate modelling for nacelle applications. In this respect, only low order models that use Kriging interpolation for regression-type functions have been used for design and optimisation [33,37,38]. Tejero et al. [33] developed an adapted method that combines RANS data and low order modelling. Relative to the expensive full CFD in-the-loop strategy, it was demonstrated that the overall computational overhead can be reduced by 50% for compact 3D non-axisymmetric configurations. Fang et al. [37] carried out the multi-objective optimisation of a non-axisymmetric nacelle with L_{nac}/r_{hi} = 3.5. The process comprised a design space exploration capability, a surrogate modelling module to build Kriging interpolation models and a genetic algorithm for the MOOs. Zhong et al. [38] developed a tool for laminar flow nacelle design. The method included a DOE capability, RANS simulations, a Kriging method as machine learning technique and the adaptive simulated annealing (ASA) algorithm [39]. The design objective was to maximise the delay of boundary layer transition at transonic conditions with M_∞ = 0.78. The overall process resulted in a new configuration with 7% larger laminar area than the baseline geometry.

Whilst different neural networks have been used for several aerodynamic applications, their combination to model aspects such as regression, classification or flow field prediction have not been considered within an overall design process. In the context of optimisation for compact ultra-high bypass ratio aero-engine nacelles this may be required to ensure low values of mid-cruise drag (regression), meet off-design requirements (classification) and guarantee specific flow field topologies (feature prediction). In this respect, the novelty of this paper is in the development of a set of neural network modelling capabilities to drive the optimisation process for transonic applications while ensuring aerodynamic robustness of the identified configurations. To assess the overall computational method, the derived nacelle geometries are compared with the ones obtained from a computationally expensive CFD in-the-loop optimisation approach.

2. Methodology

This work is based on the method developed by Tejero et al. [32,40] for the aerodynamic analysis of civil aero-engine nacelles. The design process can define a parametric nacelle geometry, perform CFD simulations or interrogate low order models to evaluate the drag, and carry out a multi-point, multi-objective optimisation. A detailed description of the different modules that compose the approach were previously provided [32,40]. Therefore, only a brief description of the methods is given in this paper.

The design process incorporates a parametric nacelle definition based on the Class-Shape Transformation (CST) method [41], which has been adapted by Christie et al. [42,43] to use intuitive design parameters [30]. The shape of a nacelle aero-line is controlled with 7 intuitive variables: $r_{hi}, L_{nac}, r_{te}, r_{if}, f_{max}, r_{max}$ and β_{nac} (Fig. 2a) [32]. The grids are multiblock structured [44] (Fig. 2b), and the viscous and compressible steady Favre-averaged Navier-Stokes equations are solved with Ansys Fluent [45] using a double-precision, implicit and density-based method (Fig. 2c). The $k-\omega$ Shear-Stress Transport (SST) turbulence model [46] with a Green-Gauss node based scheme and a second-order upwind spatial discretisation is used. The thermal conductivity is computed with the kinetic theory and the Sutherland's law is employed to calculate

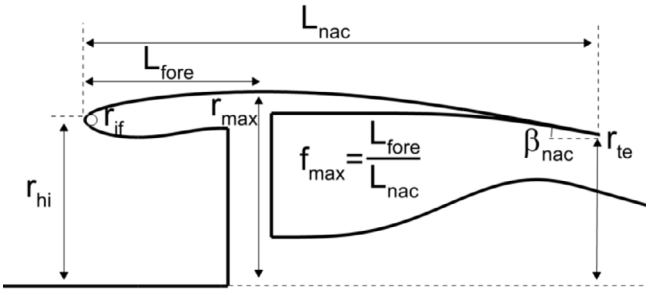

(a) Intuitive design variables used in the nacelle parametrisation

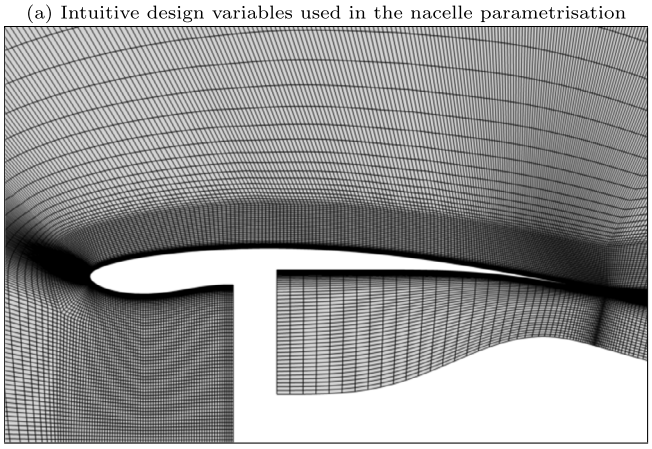

(b) Mesh detail of the computational domain

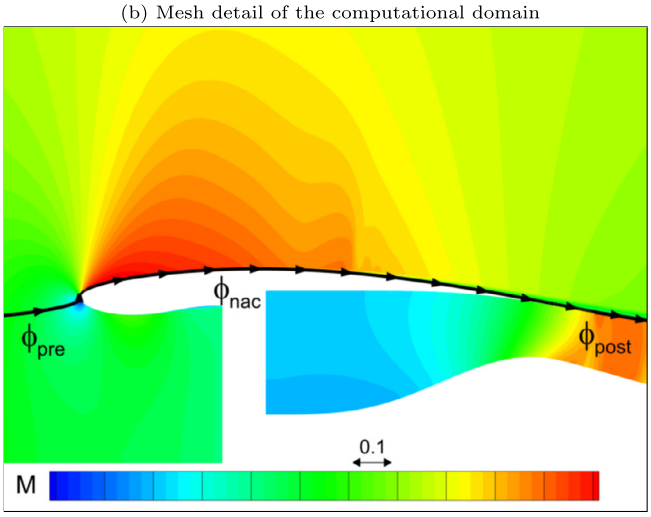

(c) Example of CFD solution for mid-cruise conditions

Fig. 2. Overview the computational methodology.

the dynamic viscosity [47]. The nacelle drag characteristics are computed with a modified near-field method [32] based on an industrial standard thrust-drag accounting approach [48]. The multi-point, multi-objective optimisation can be driven by CFD evaluations or by low order models. For previous surrogate-based studies the process was driven by Kriging interpolation response surface models [40], and the capability with neural networks has been added for this investigation. The Optimized Multi-Objective Particle Swarm Optimization (OMOPSO), developed by Sierra and Coello [49], is used for the multi-point, multi-objective investigation due to its proven capabilities for global optimisation [50,51]. This is a gradient-free method and, as such, the optimisation routine starts with a design space exploration instead of a single initial geometry as for gradient-based algorithms. The influence of the initial design space exploration on the optimal design space identified by the OMOPSO method was investigated by Sanchez-Moreno et al.

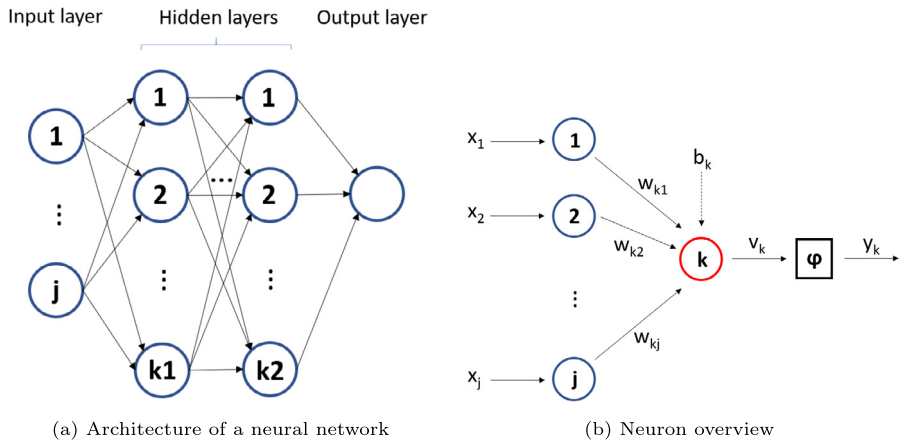

(a) Architecture of a neural network (b) Neuron overview

Fig. 3. Overview of artificial neural network architecture. Based on Goodfellow et al. [60].

[52] in nacelle applications. A total of 16 independent optimisations were performed with different design space explorations and it was demonstrated that OMOPSO has a low variability to find the optimal design space and has a reasonable convergence rate. It outperformed the genetic algorithms NSGA-II and IBEA [52].

The computational approach has been extensively used in the past for sensitivity analysis as well as numerical CFD validations were performed [32]. The grid convergence was calculated for different mesh sizes with approximately 40k, 70k and 145k cells. The mesh size with 70k cells had a GCI of 0.3% on nacelle drag and was selected for this study. The accuracy of the computational approach has been quantified with available experimental data for 2D axisymmetric nacelle configurations. The study covered a wide range of Mach numbers (0.65<M<0.95) and MFCR (0.40<MFCR<0.76). It was determined that across the cruise segment the nacelle drag was typically within 3.5% of the measured data [32].

2.1. Neural network method

For this study, a range of different neural networks are used to drive the optimisation process. They account for the non-linearity associated with transonic aerodynamics and reduce the overall computational cost of a multi-point, multi-objective optimisation with respect to a full CFD in-the-loop approach. The data to build the response surface models is gathered with a Design Space Exploration (DSE). Within the context of computer experiments, several techniques can be used to populate the design space. A review of different space-filling techniques has been summarised by Pronzato [53]. Among different space filling methods such as random, full-factorial or Latin Hypercube sampling (LHS), the LHS technique [54] was used in this study to efficiently cover the design space. This investigation considers a relatively low dimensional space and the sampling technique of LHS is adequate. However, it is important to emphasise that as the dimensionality of the problem increases more advances methods, e.g. adaptive sampling techniques, should be considered. Other sampling techniques such as adaptive space filling approaches may be computationally more efficient than the used standard LHS method [55]. However, the aim of this study is to provide initial guidelines regarding the influence of the number of samples on the prediction accuracy. For this work, a set of independent design space explorations based on LHS with different number of samples have been considered. Based on the CFD evaluations from the DSE, a range of neural networks are generated to drive the nacelle optimisation. These include capabilities for the prediction of nacelle drag integral values (regression-type), for the identification of flow characteristics (classification-type), and for the estimation of flow-fields.

Within the context of neural network architectures, the first and last layers are the input and output layers, respectively (Fig. 3a). The ones in the middle are the hidden layers (Fig. 3a) and their number depends on the complexity of the system that is going to be modelled [56]. ANNs can be classified into two main groups: (a) feed-forward NNs in which the signal flows strictly from the input to the output layer and (b) recurrent NNs that allow for feedback loops between neurons. For this work a Multi-Layer Perceptron (MLP) [57] has been used, which is a class of feed-forward ANNs.

In ANNs a neuron is connected with all of those in the previous layer through weight coefficients (Fig. 3b) [58]. The output of a neuron k can be computed as:

$$u_k = \sum_{j=1}^{m} w_{kj} x_j \tag{1}$$

Where x_j and w_{xj} are the input signals and the weighting coefficients coming from the j neurons in the previous layer, and u_k is the sum of the weighted inputs to the neuron k. For the model to achieve a better fit of the given data, a constant parameter for each neuron is added which is called bias b_k [58]. Additionally, an activation function (φ) is used to limit the neuron output amplitude (y_k) [58,59].

$$y_k = \varphi(v_k) = \varphi(u_k + b_k) \tag{2}$$

The selection of the activation function depends on the complexity of the system that is modelled. The Rectified Linear unit (ReLu) activation function (Eq. (3)) is commonly used for MLP due to its simplicity [60]. However, this activation function provides a gradient equal to 0 for every $v_k < 0$ [61], which can prevent learning as the neuron is not activated throughout the back-propagation process [62].

$$f_{relu}(v_k) = max(0, v_k) \tag{3}$$

Other activation functions use logistic equations due to their balance between linear and nonlinear behaviour [61]. They can be divided into (a) the sigmoid activation function (Eq. (4)) that spans from 0 to 1 and (b) the hyperbolic tangent activation function (Eq. (5)) which spans from -1 to 1. A well-known drawback of these logistic functions is that the gradients at the bounds tend to 0 [63]. This is known as the vanishing gradient problem and slows down the network training because the weights and biases are barely changed during the back-propagation process [63].

Table 1
Neural network hyperparameters considered.

Hyperparameter	Range
Neurons	8, 16, 32, 64, 128, 256
Hidden layers	1, 2, 3, 4, 5
Activation functions	ReLu, sigmoid, tanh

$$f_{sigmoid}(v_k) = \frac{1}{1+e^{-v_k}} \tag{4}$$

$$f_{tanh}(v_k) = tanh(v_k) \tag{5}$$

Training the networks consist on finding the set of neuron weights and biases that minimises a cost function [64]. Different cost functions can be used depending on the particular application. During the training of neural networks for integral nacelle drag and flow-field prediction, the relative root mean square error (σ_{C_D}, Eq. (6)) was selected. An accuracy function, which calculates how often predictions equal labels, was used for classification-type NNs.

$$\sigma_{C_D} = \sqrt{\frac{1}{N}\sum_{i=1}^{N}\left(\frac{C_D^{CFD} - C_D^{ANN}}{C_D^{CFD}}\right)^2} \tag{6}$$

The gradient descent ADAM optimiser was used for the training the neural networks due to its fast convergence, computational efficiency and suitability for problems with large datasets and parameters [65]. A potential problem that arises when training neural networks is the overfitting of the data. This not only happens when the architecture of the network is oversized and too many neurons and hidden layers are used but also when too many back-propagation cycles are conducted in the training process [66]. This leads to a generalisation problem where the network is not able to predict accurately the output for a different dataset than the training one [66]. For this reason, an independent dataset for validation is compiled to quantify the accuracy of the NN surrogate models, and is also generated with a Latin Hypercube Sampling (LHS).

Different hyperparameters are considered during the training of the NNs (Table 1). A full factorial for the different combinations of hyperparameters is performed to tune the surrogate models. The selection of the NNs is based on the minimum prediction error in the independent dataset.

3. Results and analysis

This investigation is based on a compact nacelle configuration envisaged for future civil aero-engines [67] with a fixed normalised nacelle length of L_{nac}/r_{hi} = 3.1, and four intuitive variables (r_{max}, r_{if}, f_{max} and β_{nac}) vary during the optimisation process (Fig. 2a). Different flight conditions that are encountered during the flight envelope are considered to ensure aerodynamic robustness of the derived nacelle shapes. They are mid-cruise, perturbations to assess the sensitivity to flight Mach number and MFCR as well as an off-design windmilling diversion scenario (Table 2). This range of transonic conditions presents a significant challenge for the optimisation process due to the high non-linearity of the problem considered (Fig. 1). For this study, the nacelle drag (Eq. (7)) for the conditions encountered during the cruise segment (mid-cruise, increased Mach number (iM) and end-of-cruise (EoC) in Table 2) is minimised during the MOO, and a classification criteria was set for the diversion case. As a threshold for the classification metric, it was defined that designs exhibiting an axial extent of boundary layer separation larger than 10% of the nacelle length ($L_{sep}/L_{nac} = 0.1$) at windmilling diversion were not acceptable, and

Table 2
Flight conditions considered during the multi-point, multi-objective nacelle optimisation process.

Condition	Mach No.	MFCR	type
$mid-cruise$	0.85	0.70	regression
iM	0.87	0.70	regression
EoC	0.85	0.65	regression
$diversion$	0.65	<0.5	classification

therefore, were excluded of the optimisation process. Schreiner et al. [34] identified a weak linear correlation between the drag at mid-cruise and windmilling diversion conditions. The study was based on the multi-point, multi-objective optimisation of a compact aero-engine nacelle in which the mid-cruise as well as diversion were regression metrics. It was found that some CFD effort during the optimisation routine was focused on regions of the design space with low cruise drag but unreasonable large drag at diversion. For this reason, this work uses the diversion condition with a classification metric to reduce the CFD overhead of the optimisation and target likely optimal regions of the space.

$$C_D = \frac{D_{nac}}{\frac{1}{2}\rho_\infty V_\infty^2 A_{hi}} = \frac{\phi_{pre}+\phi_{nac}+\phi_{post}}{\frac{1}{2}\rho_\infty V_\infty^2 A_{hi}} \tag{7}$$

3.1. MOO with a CFD in-the-loop approach

To establish a baseline for the surrogate-based optimisation with neural networks, a MOO was performed with an expensive CFD in-the-loop approach. The process is started with a design space exploration based on a LHS in which 400 nacelle designs are evaluated by numerical simulations. Following generations of the genetic algorithm are formed of 50 designs. The hypervolume of the Pareto front is monitored and the process is stopped when the hypervolume changes less than 1% in three consecutive generations. The design process is driven with the three regression-type objectives functions (Table 2), in which the nacelle drag for $C_{D-cruise}$, C_{D-iM} and C_{D-EoC} is minimised. In addition, it is ensured that the prescribed maximum axial extent of the separated flow region along the fancowl ($L_{sep}/L_{nac} < 0.1$) is achieved for the windmilling diversion scenario. As such, this off-design condition is used as a classification function. The multi-point, multi-objective optimisation results in a three dimensional Pareto front that can be represented with a 2D projection on the $C_{D-cruise}$ and C_{D-iM} space and coloured by C_{D-EoC} (Fig. 4). It highlights the trade-off between the different flight conditions considered. Four different configurations have been downselected to provide a better insight into the aerodynamics of compact aero-engine nacelles. They are the design with minimum $C_{D-cruise}$ (A1), C_{D-iM} (A2), C_{D-EoC} (A3) and a trade-off between the three objectives functions (A4). Relative to A1, the mid-cruise increases by 5.6%, 6.1% and 2.8% for A2, A3 and A4, respectively. The design with minimum $C_{D-cruise}$ has a penalty of 16.7% in nacelle drag at an increased Mach number (C_{D-iM}) compared with A2. This changes to 36.0% and 7.3% for A3 and A4, respectively. This variability demonstrates the large sensitivity of compact nacelles with L_{nac}/r_{hi} = 3.1 to an increased flight Mach number of M = 0.87. The design A1 has a 3.2% larger drag at end-of-cruise (C_{D-EoC}) relative to A3, which increases to 8.7% and 6.9% for A2 and A4, respectively.

The changes on the nacelle drag characteristics for the designs in the Pareto front are accompanied by differences in the associated flow characteristics (Fig. 5). While the designs A1 and A3 have a single shock, the nacelles A2 and A4 present a double shock structure. All four designs have a shock at $X/L_{nac} \approx 0.50$ but a different pre-shock Mach number. Relative to the configuration A1 (lowest $C_{D-cruise}$), the designs A2 and A3 have an increment in

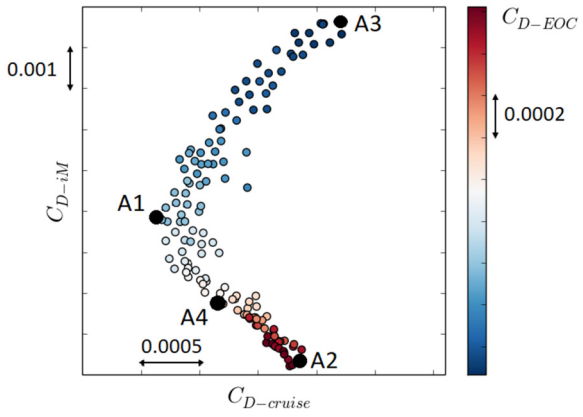

Fig. 4. Pareto front identified with the CFD in-the-loop method.

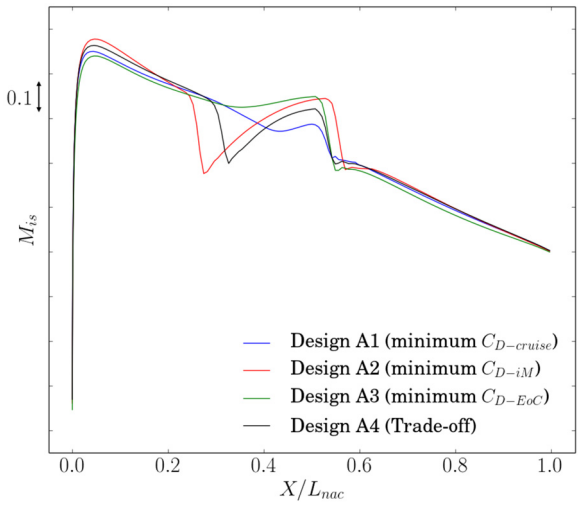

Fig. 5. M_{is} distribution for downselected designs from the CFD in-the-loop method.

pre-shock M_{is} of 0.075 and the nacelle A4 of 0.03. There are also differences in the initial flow acceleration around the nacelle lip which results in changes of peak M_{is}. Relative to the design A1, the peak M_{is} increases by 0.03 and 0.015 for A2 and A4 and reduces by 0.01 for A3.

This CFD in-the-loop approach accounts for cruise-type conditions and a windmilling diversion scenario in which regression and classification metrics are used. This is to ensure aerodynamic robustness for key operating points. Although the CFD in-the-loop optimisation has resulted in a well-populated Pareto front (Fig. 4), this has a relatively large computational cost. For this reason, there is a desire to expand the nacelle design approach to a surrogate-based optimisation method.

3.2. MOO with neural networks

3.2.1. Effect of sample size on predictive accuracy

A key aspect of surrogate modelling is to define an adequate number of samples to build the RSM. This should be based on the trade-off between an acceptable predictive accuracy and the cost to build the model. In this respect, four independent design space explorations based on a LHS of 100, 200, 400 and 800 nacelle designs were considered as inputs for the NN models. This gives a ratio between the number of samples and degrees of freedom (N_s/N_{DOF}) of 25, 50, 100 and 200. The total computational cost of generating these databases is approximately 6.25%, 12.5%, 25.0% and 50.0% relative to the full CFD in-the-loop optimisation. An independent set of 400 nacelle configurations, also based on the LHS technique, was compiled to assess the predictive accuracy of the different neural networks.

For the different databases (N_s = 100, 200, 400 and 800), a range of NNs were built to predict the nacelle drag across the design space for the regression objective functions, i.e. $C_{D-cruise}$, C_{D-iM} and C_{D-EoC} (Table 2). The full factorial combination of hyperparameters presented in Table 1 were considered to tune the models and reduce the predictive uncertainty. A cross-validation of each NN with the independent nacelle data was performed to quantify the relative root mean square error (σ_{C_D} as defined in Eq. (6)) on the nacelle drag model's prediction. As an example, Fig. 6 shows the effect of the different hyperparameters on the nacelle drag uncertainty for the database with N_s = 400. It highlights that the active function selection has a large impact on the model accuracy for the three objective functions of interest ($C_{D-cruise}$, C_{D-iM} and C_{D-EoC}). For this non-linear data, the ReLu function (Eq. (3)) gives lower values of σ_{C_D} than sigmoid (Eq. (4)) and tanh (Eq. (5)). For example, for mid-cruise conditions ($C_{D-cruise}$), the minimum achievable σ_{C_D} is 2.5%, 3.9% and 3.8% for ReLu, sigmoid and tanh, respectively. Within the generated NNs with the ReLu function, it was observed that an appropriate selection of neurons per hidden layer is needed to achieve low values of nacelle drag relative root mean square error. The best performing NNs were obtained when the network was formed by 64 or 128 neurons per hidden layer. This was consistently found for the three operating points (Fig. 6). Conversely, the total number of hidden layers for the NN architecture has a relatively low impact on the drag uncertainty. For example, for the mid-cruise low order models with a fixed ReLu activation function and 128 neurons per hidden layer, a variation in the total number of hidden layers between 1 and 5 changes σ_{C_D} between 2.5% and 3.2%. The same relative importance of the three hyperparameters, i.e. activation function, neurons per hidden layer and total number of hidden layers, was found for the other databases with N_s=100, 200 and 800 designs.

The NN architectures with the minimum relative root mean square (σ_{C_D}) on the predicted nacelle drag of each condition ($C_{D-cruise}$, C_{D-iM} and C_{D-EoC}) and sample size (N_s = 100, 200, 400 and 800) was identified (Fig. 7). For the three flight regimes there is a pronounced reduction on σ_{C_D} when N_s increases from 100 to 200. The relative root mean square error asymptotically reduces for $N_s > 200$. For example, an increment by a factor of two in the CFD overhead to generate N_s = 800 relative to N_s = 400, only reduces σ_{C_D} by 0.14%, 0.20% and 0.10% for $C_{D-cruise}$, C_{D-iM} and C_{D-EoC}, respectively. For a fixed N_s the greatest predictive error is always found for C_{D-iM}, due to the larger non-linearity at this relatively high Mach number (M = 0.87). For this study the acceptable threshold in terms of predictive accuracy is defined at σ_{C_D}=5.0%, which was demonstrated to predict the gradients across the design space for 2D axisymmetric low order models in nacelle applications [40]. As such, the NNs generated with N_s=100 do not meet the criteria and are not consider further in this investigation. To provide an insight of the cross-validation, Fig. 8 shows a comparison between the CFD and the NN generated with N_s = 400 for mid-cruise conditions ($C_{D-cruise}$). It shows the good predictive capability of the low order model with a relative root mean square error (σ_{C_D}) of 2.5% in which there are no designs that have a prediction error above 10% and only 2.0% of the designs have $\sigma_{C_D} > 5\%$.

Previous investigations have highlighted that compact nacelles are more sensitive to off-design windmilling conditions compared with conventional architectures [34]. As previously described, a diversion windmilling condition is used during the multi-point, multi-objective optimisation process to improve the aerodynamic robustness of the derived nacelle configurations (Table 2). This flight condition has been treated with a classification approach in which the axial extent of the boundary layer separation was lim-

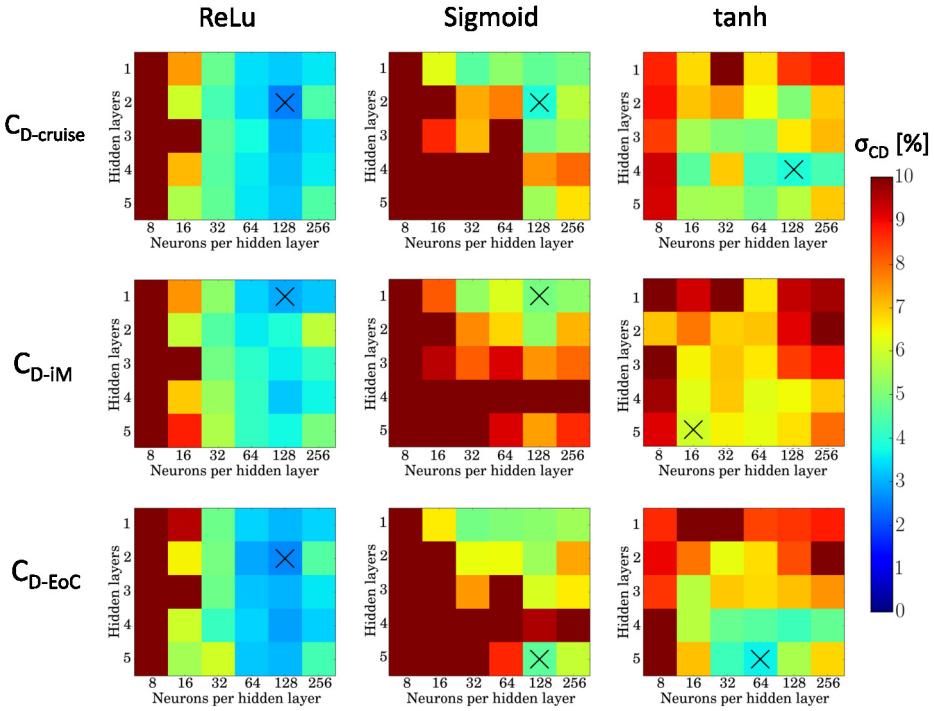

Fig. 6. Influence of the neural network hyperparameters on the nacelle drag prediction (regression) for the database compiled with N_s=400. The symbol × marks the minimum σ_{C_D} value.

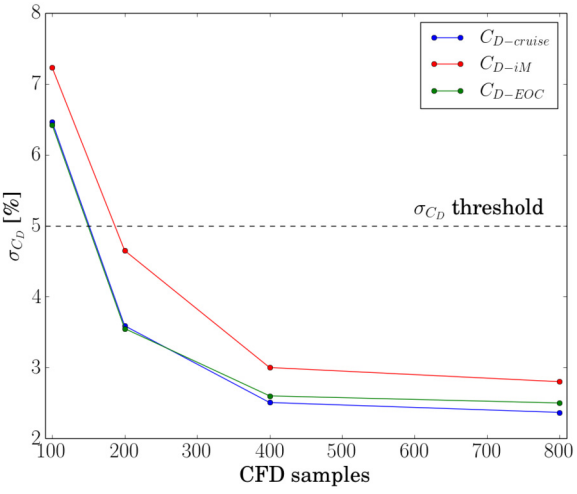

Fig. 7. Effect of N_s sampling on predictive accuracy for $C_{D-cruise}$, C_{D-iM}, C_{D-EoC}.

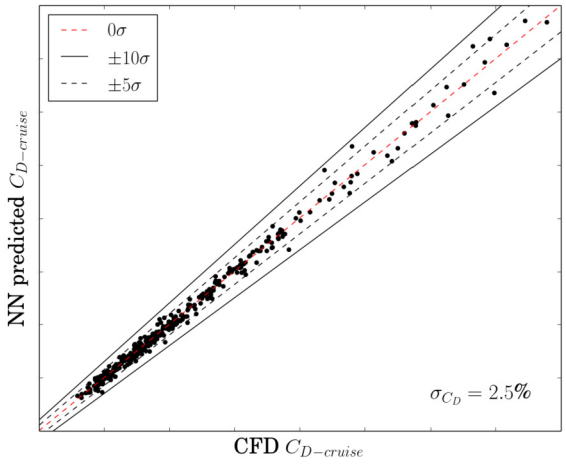

Fig. 8. Example of cross-validation for the regression neural network at mid-cruise conditions for the database compiled with N_s=400.

ited to a maximum of 10% of the nacelle chord (L_{sep}/L_{nac} = 0.1). The training process for the classification neural network is based on maximising the predictive accuracy across the design space for which the NN and CFD predictions are equal, i.e. both predict that the axial extent of flow separation is below or above 10% of L_{nac}. However, it is important to note that an optimisation process driven by a low order model with a classification approach should also reduce as much as possible the false-positives, i.e. designs for which the CFD predicts flow separation larger than $0.1 \cdot L_{nac}$ and the NN predicts that the criterion in the maximum L_{sep}/L_{nac} is met. This is to ensure that the optimisation process is not driven to regions of the design space which are not feasible due to the imposed classification requirement. A set of classification-type NNs were generated for the databases N_s=200, 400 and 800. Only the sigmoid function was considered because the NN output can be interpreted as a probability distribution function [61]. A full factorial combination was performed for the other hyperparameters, i.e. neurons per hidden layer and total number of hidden layers. Fig. 9 presents the predictive accuracy of the generated NNs in which the colour indicates the percentage of designs in which NN and CFD labels are the same and the number marks the false-positives. Whilst the regression-type NNs presented a large influence of the number of neurons per hidden layer in the model's uncertainty (Fig. 6), this was not identified for the classification-type NNs (Fig. 9). Overall, increasing the sample size from 200 to 800 increases the predictive accuracy and reduces the number of false-positives. For the best NN architectures identified during the full factorial combination of hyperparameters, it was found that the overall classification accuracy of the NN models was 96%, 97% and 98% with 8, 3 and 0 false-positives for the models built with N_s = 200, 400 and 800, respectively (Fig. 9). The designs which were wrongly classified were assessed at mid-cruise conditions to evaluate the effect of this wrong prediction within an optimisation process. For the NN model generated with N_s=200

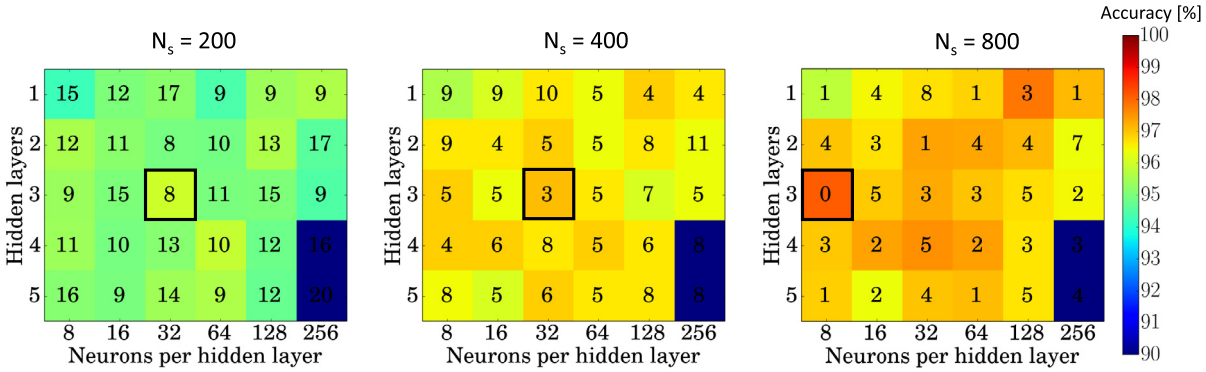

Fig. 9. Influence of the neural network hyperparameters on boundary layer flow separation classification for the windmilling diversion scenario. The symbol □ marks the maximum accuracy.

in which 8 designs were false-positives, one nacelle design exhibited a 2.0% greater cruise drag relative to the minimum drag identified in the design space exploration. This is within the uncertainty of the $C_{D-cruise}$ regression model, i.e. $\sigma_{C_D} = 3.5\%$ (Fig. 7). Therefore, it was concluded that the RSMs generated with N_s = 200 may not be suitable for use within an optimisation process. Conversely, the three false-positive designs from the NN generated with N_s=400 had a mid-cruise drag above 20% of the minimum value identified in the DSE. As such, it is not expected that these configurations will be identified during a multi-point, multi-objective optimisation. This confirms the suitability of this low order model with N_s = 400 for aero-engine nacelle optimisation studies.

It is important to note that, for a targeted accuracy of the ANN, the number of samples compiled during the design space exploration will increase with the dimensionality of the problem. For very high number of dimensions, the developed method in this work may have limitations. As such, for high dimensional spaces, this approach may be combined with dimensionality reduction techniques to ensure a tractable method to build low order models. For this purpose, feature extraction or feature selection could be used. In particular, the design and optimisation strategy developed by Lopez et al. [9] has been demonstrated to be a feasible approach due to its proven scalability capabilities.

3.2.2. Flow prediction neural network

Aerodynamic shape design is a multidisciplinary discipline where the process is guided not only from aerodynamic considerations but also from other constraints imposed by aero-structural or aero-acoustical requirements [68]. For the investigated design space of compact aero-engine nacelles, small changes in the geometric shape can lead to large differences in the drag and associated flow features. For this reason, a neural network capability was developed to predict the isentropic Mach number distribution along the fancowl. As previously, the hyperparameters were also tuned to minimise the relative root mean square error on the M_{is} prediction ($\sigma_{M_{is}}$). A full factorial of the different hyperparameters combinations presented in Table 1 was considered for the different models built with N_s=200, 400 and 800. For these neural networks with different N_s values, it was found that the activation function does not have a large impact on the model's accuracy. For example, Fig. 10 shows the effect of the different hyperparameters for the database compiled with 400 samples. For a fixed number of hidden layers and neurons per hidden layer, the three activation functions (ReLu, sigmoid and tanh) have similar $\sigma_{M_{is}}$. Across the range of hyperparameters, the lowest $\sigma_{M_{is}}$ was approximately 1.1%, 1.3% and 1.2% for the activation functions ReLu, sigmoid and tanh, respectively. As for previous regression-NNs, ReLu has the best prediction capabilities. The same conclusion was obtained for the other N_s values of 200 and 800, in which the best performing network had $\sigma_{M_{is}}$ = 1.4% and 0.9%, respectively.

A wide range of different flow-field characteristics are encountered in the investigated design space of this compact aero-engine nacelle with L_{nac}/r_{hi} = 3.1. For example, there may be configurations that have strong initial acceleration around the nacelle lip with a first shock wave on the nacelle forebody and a re-acceleration to terminate in a second shock on the afterbody [32]. Other nacelle architectures may present a more controlled acceleration around the nacelle lip to terminate in a single strong shock around the nacelle crest or there may be configurations without a shock wave [32]. To demonstrate the capability of the NNs, the isentropic Mach number prediction along the nacelle for a set of configurations is presented in Fig. 11. This is carried out for perturbations in the two key design variables of r_{max} and f_{max}, which have large impact on the nacelle drag and aerodynamic characteristics [32]. Whilst the NN derived with N_s = 200 has errors in the peak M_{is} and shock location prediction, the other two NNs compiled with N_s = 400 and 800 are able to predict the peak and pre-shock M_{is} within 0.01 and shock location within $0.02 \cdot L_{nac}/r_{hi}$.

For the downselected NNs with N_s = 200, 400 and 800, their predictive uncertainty across the design space was also quantified with a statistical analysis of the M_{is} prediction error along the fancowl chord. Fig. 12 presents the relative root mean square prediction on isentropic Mach number as a function of the nacelle length (X/L_{nac}). The NNs with N_s = 400 and 800 have similar relative root mean square error ($\sigma_{M_{is}}$). For the initial nacelle forebody with $X/Lnac < 0.1$ and the nacelle aft end with $X/Lnac > 0.8$, $\sigma_{M_{is}}$ is below 0.8% and 0.4%, respectively. A slightly greater uncertainty arises in the region of $0.1 < X/Lnac < 0.8$ due to the expected errors in accurately identifying the shock locations, in which there is a maximum $\sigma_{M_{is}}$ of approximately 1.6%. This increases to $\sigma_{M_{is}}$ = 2.0% when the neural network is trained with 200 samples (Fig. 12).

It has been demonstrated that building neural networks with N_s = 200, 400 and 800, i.e. N_s/N_{DOF} = 50, 100 and 200, results in adequate regression metamodels for nacelle drag prediction (Fig. 7). They meet an acceptable prediction uncertainty of $\sigma_{C_D} <$ 5% [40] across the three operating conditions of interest ($C_{D-cruise}$, C_{D-iM} and C_{D-EoC}). However, the NN with N_s = 200 showed a larger uncertainty in the boundary layer flow separation classification of nacelles under windmilling diversion conditions (Fig. 9) as well as limited capabilities to predict the associated flow-field characteristics (Fig. 11). Although the low order models generated with N_s=800 are more accurate than those with N_s=400 (Fig. 7, 9 and 12), the relative improvements are modest in comparison with the greater CFD cost. Based on this consideration, it was concluded

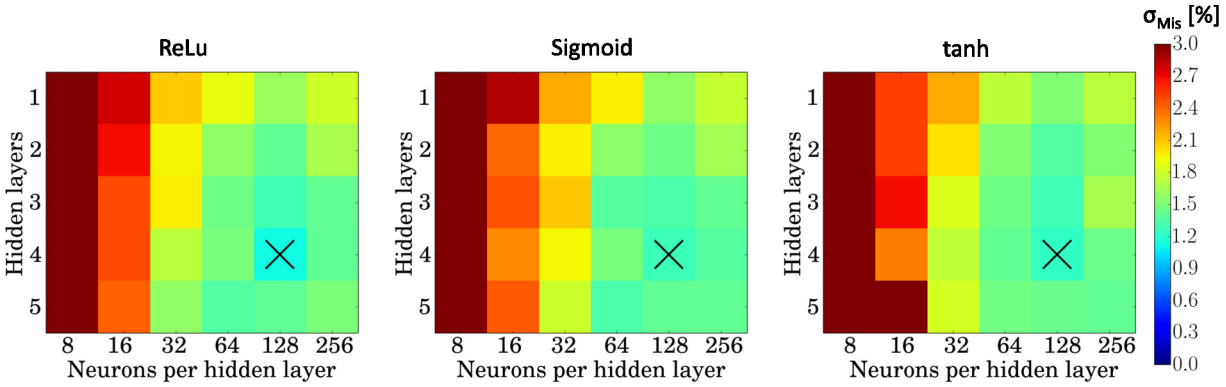

Fig. 10. Influence of the neural network hyperparameters on the M_{is} prediction for the model compiled with N_s=400. The symbol × marks the minimum $\sigma_{M_{is}}$ value.

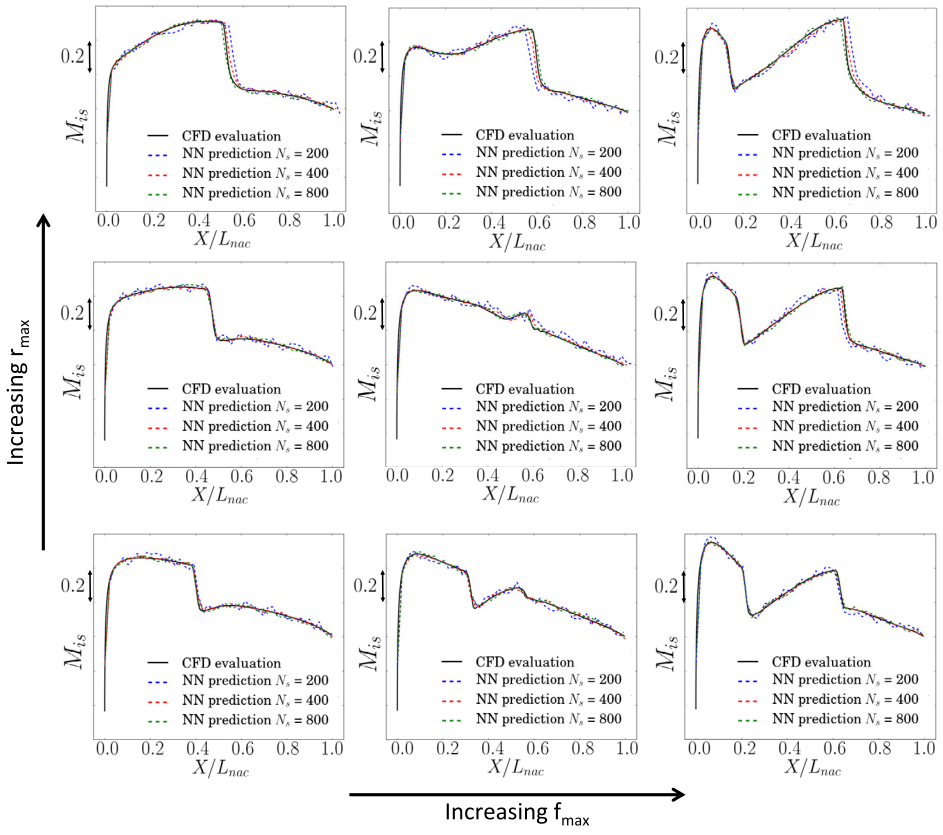

Fig. 11. Neural network for M_{is} prediction at mid-cruise conditions across the design space.

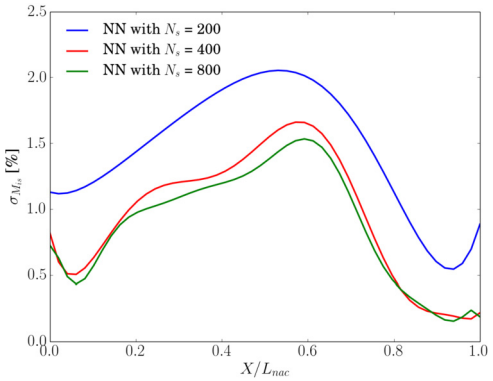

Fig. 12. Statistical analysis of the predictive uncertainty on M_{is} as a function of the nacelle axial location.

Table 3
Final Hyperparameters for the models generated with N_s=400.

Hyperparameter	*mid − cruise*	*iM*	*EOC*	*diversion*	*Flow − field*
Neurons	128	128	128	32	128
Hidden layers	2	1	2	3	4
Activation functions	ReLu	ReLu	ReLu	sigmoid	ReLu

that the accuracy of the NNs generated with N_s=400 was sufficient for the design and optimisation of compact civil aero-engine nacelles. A summary of the hyperparameters that were used to compile the different surrogate models with N_s=400 is presented in Table 3.

3.2.3. Nacelle design and optimisation

Having established confidence in the predictive accuracy of the neural networks, the models (Table 3) were applied within an op-

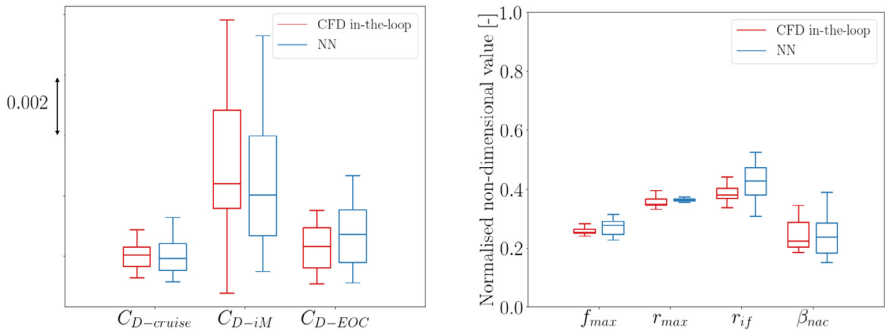

(a) Performance metric (b) Design variables

Fig. 13. Pareto front comparison for a CFD in-the-loop and NN optimisation strategy.

timisation environment to carry out nacelle design studies. The optimisation outcomes obtained with the NNs are compared with the results from the computationally expensive CFD in-the-loop approach (Section 3.1). The optimisation process also started with a design space exploration based on a LHS of 400 designs which were evaluated with the derived NNs (Table 3). Subsequent generations from the OMOPSO algorithm used 50 designs and the process was monitored with the Pareto front hypervolume change to ensure a variation lower than 1% in the last three generations. The optimisation process was driven by minimising the nacelle drag using the three regression NNs ($C_{D-cruise}$, C_{D-iM}, C_{D-EOC}), and one classification NN to ensure that the diversion requirement of axial extent of boundary layer separation was below 10% of the nacelle length.

A comparison between the CFD in-the-loop and surrogate-based optimisation for the performance metrics and design variables of the individuals within the Pareto front is presented in Fig. 13. It shows that both key aspects in a design process can be predicted by the proposed neural network strategy. The minimum $C_{D-cruise}$ identified with the low order model was slightly underpredicted relative to the CFD strategy by around 1% whereas the mean value was within 0.5%. Similar outcomes were identified for the spillage drag ($C_{D-spill}$) (Fig. 13a). Slightly larger differences arise for the nacelle drag at an increased Mach number (C_{D-iM}) caused the by higher non-linearity at an increased Mach number and the greater predictive uncertainty of the model (Section 3.2.1). For example, the minimum C_{D-iM} identified by the surrogate-based optimisation was 2.8% larger than the one from the CFD in-the-loop strategy. Other key aspect of the presented approach is that the design variables of the optimal design space are well predicted by the surrogate-based strategy (Fig. 13b). The plot is normalised with the bounds of each design variable where 0 and 1 refer to the optimisation lower and upper bound, respectively. The CFD in-the-loop optimisation required the initial design space exploration (DSE) of 400 designs and 30 subsequent generations of 50 designs each. Conversely, the NN optimisation was only based in an initial sampling with N_s=400. As such, the proposed nacelle optimisation with neural networks reduces the computational cost by approximately 75% compared to the CFD in-the-loop strategy.

In the context of surrogate-based optimisation, other key requirement is that the flow physics of possible downselected configurations are similar to the ones derived from a CFD in-the-loop strategy. As previously described, a capability to predict M_{is} distributions with neural networks has been developed. In this context, four configurations from the surrogate-based optimisation were downselected to cover different criteria: minimum $C_{D-cruise}$ (design B1), minimum C_{iM} (design B2), minimum $C_{D-spill}$ (design B3) and a trade-off between the three objectives functions (design B4). This downselection process is the same as the one that was previously followed for the configurations "A" from the CFD in-the-loop optimisation method (Fig. 5). The isentropic Mach number distribution for the designs B were predicted with the NN low order model described in Section 3.2.2 (Fig. 14). The downselected B designs have the same flow characteristics as the A configurations in terms of number of shock-waves, their location and pre-shock M_{is}. For the nacelles with minimum $C_{D-cruise}$ (A1 and B1) a similar shock location was identified but the pre-schock Mach number increases by 0.02 for the surrogate-based MOO (Fig. 14a). The designs A2 and B2, lowest C_{D-iM}, depict a double shock structure in which the first shock-wave appears at X/L_{nac} = 0.25 and the flow reaccelerates and terminates with a second shock at around $X/L_{nac} \approx 0.50$. Both designs (A2 and B2) have the same shock locations and pre-shock M_{is} (Fig. 14b). Similar outcomes were identified for the designs A3-B3 and A4-B4, i.e. minimum C_{D-EOC} and trade-off design, respectively (Figs. 14c and 14d). As such, it is proven that the NN based method is also able to identify and predict the same flow physics of downselected configurations as those from a more computationally expensive CFD in-the-loop optimisation.

The findings reported in this work are for a compact nacelle with L_{nac}/r_{hi} = 3.1, which is expected for future civil aero-engines. The design space considered is a challenging problem due to the non-linearity associated with transonic aerodynamics. As such, it is expected that the reported performance of the current neural network-based optimisation method is representative across the design space of compact architectures.

4. Conclusions

This article describes a design method with neural networks for transonic optimisation applications. The process uses low order models for regression, classification and flow-field prediction and is used for the design of ultra-high bypass ratio aero-engine nacelles. The approach has been coupled with a multi-point, multi-objective optimisation strategy to identify designs that are aerodynamically robust across different conditions of the flight envelope.

Relative to a computational expensive CFD in-the-loop approach, it has been demonstrated that the new developed neural network capability converges to similar optimal regions of the design space. The overall computational cost is reduced by 75% with an uncertainty in the regression performance metrics of 2.8% and a predictive accuracy for the classification metric of 98%. For the surrogate-based optimisation, the associated flow physics of downselected nacelles were evaluated with a neural network, in which the peak Mach number, shock location and pre-shock Mach number were successfully predicted with similar values to the designs derived from a CFD-based optimisation. Overall, the neural

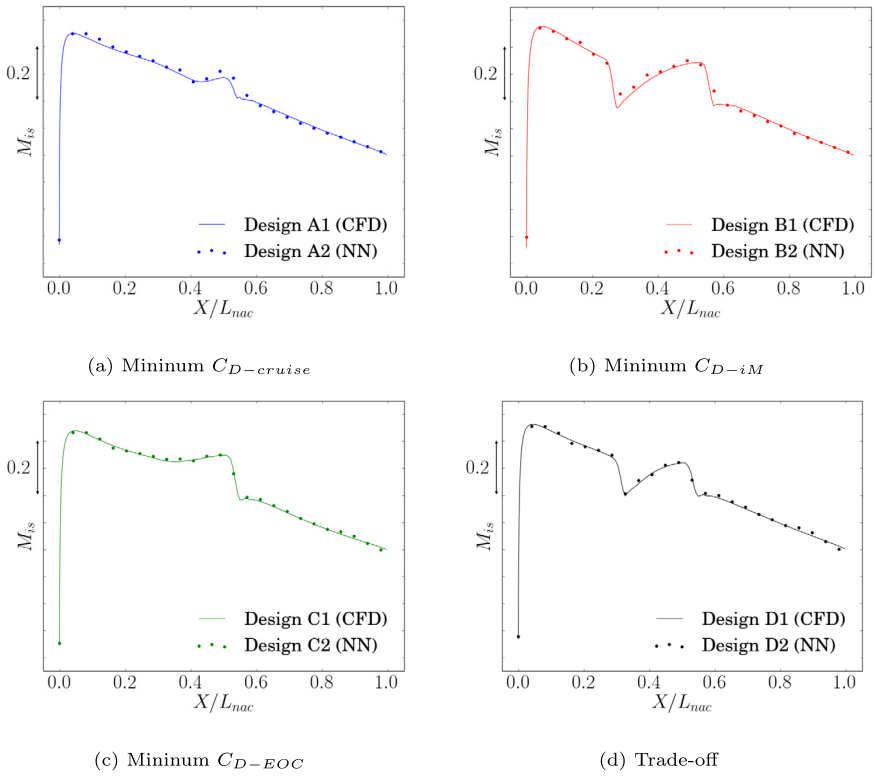

(a) Mininum $C_{D-cruise}$ (b) Mininum C_{D-iM}

(c) Mininum C_{D-EOC} (d) Trade-off

Fig. 14. M_{is} distribution for downselected designs from a CFD in-the-loop (A-label) and NN-based (B-label) optimisation strategy. The "A" designs are evaluated with CFD and the "B" designs with the NN flow-field prediction method.

network method enables the optimisation of complex non-linear aerodynamic problems in which different design requirement need to be fulfilled.

Declaration of competing interest

The authors declare that they have no known competing financial interests or personal relationships that could have appeared to influence the work reported in this paper.

Data availability

The data that has been used is confidential.

Acknowledgements

This project has received funding from the Clean Sky 2 Joint Undertaking under the European Union's Horizon 2020 Research and Innovation Program under Grant Agreement No. 820997.

References

[1] S. Skinner, H. Zare-Behtash, State-of-the-art in aerodynamic shape optimisation methods, Appl. Soft Comput. 62 (2018) 933–962.
[2] J.R. Martins, J.J. Alonso, J.J. Reuther, A coupled-adjoint sensitivity analysis method for high-fidelity aero-structural design, Optim. Eng. 6 (2005) 33–62.
[3] J. Li, S. He, J. Martins, Data-driven constraint approach to ensure low-speed performance in transonic aerodynamic shape optimization, Aerosp. Sci. Technol. 92 (2019) 536–550.
[4] H. Likeng, G. Zhenghong, Z. Dehu, Research on multi-fidelity aerodynamic optimization methods, Chin. J. Aeronaut. 26 (2) (2013) 279–286.
[5] A. Sobester, S. Powell, Design space dimensionality reduction through physics-based geometry re-parameterization, Optim. Eng. 14 (2013) 37–59.
[6] S.L. Brunton, B.R. Noack, P. Koumoutsakos, Machine learning for fluid mechanics, Annu. Rev. Fluid Mech. 52 (2020) 477–508.
[7] J. Li, X. Du, J. Martins, Machine learning in aerodynamic shape optimization, Prog. Aerosp. Sci. 134 (2022) 100849.
[8] C. Sabater, P. Sturmer, P. Bekemeyer, Fast predictions of aircraft aerodynamics using deep-learning techniques, AIAA J. 60 (9) (2022) 5249–5261.
[9] D. Lopez, T. Ghisu, S. Shahpar, Global optimization of a transonic fan blade through AI-enabled active subspaces, J. Turbomach. 144 (1) (2022).
[10] Q. Du, Y. Li, L. Yang, T. Liu, D. Zhang, Y. Xie, Performance prediction and design optimization of turbine blade profile with deep learning method, Energy 254 (2022) 124351.
[11] N.R. Secco, B.S. de Mattos, Artificial neural networks to predictaerodynamic coefficients of transport airplanes, Aircr. Eng. Aerosp. Technol. 89 (2) (2017) 211–230.
[12] D. Lopez, T. Ghisu, T. Kipouros, S. Shahpar, M. Wilson, Extending highly loaded axial fan operability range through novel blade design, J. Turbomach. 144 (12) (2022).
[13] M. Bouhlel, S. He, J. Martins, Scalable gradient-enhanced artificial neural networks for airfoil shape design in the subsonic and transonic regimes, Struct. Multidiscip. Optim. 61 (2020) 1363–1376.
[14] C. Bosson, T. Nikoleris, Supervised learning applied to air traffic trajectory classification, in: 2018 AIAA Information Systems-AIAA InfoTech, AIAA Paper 2018-1637, 2018.
[15] S. Hosder, L.T. Watson, B. Grossman, W.H. Mason, H. Kim, R.T. Haftka, S.E. Cox, Polynomial response surface approximations for the multidisciplinary design optimization of a high speed civil transport, Optim. Eng. 2 (2001) 431–452.
[16] J. Jung, H. Yang, K. Kim, K. Yee, K. You, K. Park, S. Jeong, Conceptual design of a reusable unmanned space vehicle using multidisciplinary optimization, Int. J. Aeronaut. Space Sci. 19 (2018) 743–750.
[17] S. Bhatnagar, Y. Afshar, S. Pan, K. Duraisamy, S. Kaushik, Prediction of aerodynamic flow fields using convolutional neural networks, Comput. Mech. 64 (2019) 525–545.
[18] K. Zuo, S. Bu, W. Zhang, J. Hu, Z. Ye, X. Yuan, Fast sparse flow field prediction around airfoils via multi-head perceptron based deep learning architecture, Aerosp. Sci. Technol. 130 (2022) 107942.
[19] M.M. Rai, N.K. Madavan, Aerodynamic design using neural networks, AIAA J. 38 (1) (2000) 173–182.
[20] G. Sun, Y. Sun, S. Wang, Artificial neural network based inverse design: airfoils and wings, Aerosp. Sci. Technol. 42 (2015) 415–428.
[21] A. Kharal, A. Saleem, Neural networks based airfoil generation for a given Cp using Bezier - PARSEC parameterization, Aerosp. Sci. Technol. 23 (1) (2012) 330–344.
[22] R. Derksen, T. Rogalsky, Bezier-PARSEC: an optimized aerofoil parameterization for design, Adv. Eng. Softw. 41 (2010) 929–930.

[23] R. Gupta, R. Jaiman, A hybrid partitioned deep learning methodology for moving interface and fluid–structure interaction, Comput. Fluids 233 (2022) 105239.
[24] C. Poggi, M. Rossetti, J. Serafini, G. Bernardini, M. Gennaretti, U. Iemma, Neural network meta–modelling for an efficient prediction of propeller array acoustic signature, Aerosp. Sci. Technol. 130 (2022) 107910.
[25] K. Chowdhary, C. Hoang, K. Lee, J. Ray, V. Weirs, B. Carnes, Calibrating hypersonic turbulence flow models with the HIFiRE-1 experiment using data-driven machine-learned models, Comput. Methods Appl. Mech. Eng. 401 (2022) 115396.
[26] G. Novati, H. de Laroussilhe, P. Koumoutsakos, Automating turbulence modelling by multi-agent reinforcement learning, Nat. Mach. Intell. 3 (2021) 87–96.
[27] N. Birch, 2020 vision: the prospects for large civil aircraft propulsion, Aeronaut. J. 104 (1038) (2000) 347–352.
[28] I. Goulos, J. Otter, F. Tejero, J.H. Rebassa, D. MacManus, Civil turbofan propulsion aerodynamics: thrust-drag accounting and impact of engine installation position, Aerosp. Sci. Technol. 111 (2020) 106533.
[29] D. Daggett, S. Brown, R. Kawat, Ultra-Efficient Engine Diameter Study, Tech. Rep. CR-2003-212309, NASA, 2003.
[30] F. Tejero, D. MacManus, J. Hueso-Rebassa, F. Sanchez-Moreno, I. Goulos, C. Sheaf, Aerodynamic optimisation of future civil aero-engines by dimensionality reduction and multi-fidelity techniques, Int. J. Numer. Methods Heat Fluid Flow (2022).
[31] F. Sanchez-Moreno, D. MacManus, J. Hueso-Rebassa, F. Tejero, J. Matesanz-Garcia, C. Sheaf, Optimization of installed compact and robust nacelles using surrogate models, in: 33rd Congress of the International Council of the Aeronautical Sciences: ICAS 2022, 2022.
[32] F. Tejero, M. Robinson, D. MacManus, C. Sheaf, Multi-objective optimization of short nacelles for high bypass ratio engines, Aerosp. Sci. Technol. 91 (2019) 410–421.
[33] F. Tejero, R. Christie, D. MacManus, C. Sheaf, Non-axisymmetric aero-engine nacelle design by surrogate-based methods, Aerosp. Sci. Technol. 117 (2021) 106890.
[34] B.D.J. Schreiner, F. Tejero, D. MacManus, C. Sheaf, Robust aerodynamic design of nacelles for future civil aero-engines, in: Proceedings of ASME Turbo Expo 2020: Turbomachinery Technical Conference and Exposition, 2020, pp. GT2020–GT14470.
[35] A.M. Carr, Estimation of Windmilling Drag and Airflow of Tubo-Jet and Turbo-Fan Engines, Tech. Rep. ESDU-81009, ESDU, November 1981.
[36] V.T. Silva, A. Lundbladh, O. Petit, C. Xisto, Multipoint aerodynamic design of ultrashort nacelles for ultrahigh-bypass-ratio engines, J. Propuls. Power 38 (2022) 1–18.
[37] X. Fang, Y. Zhang, S. Li, H. Chen, Transonic Nacelle Aerodynamic Optimization Based on Hybrid Genetic Algorithm, 17th AIAA/ISSMO Multidisciplinary Analysis and Optimization Conference, AIAA AVIATION Forum, AIAA Paper Number 2016-3833, 2016.
[38] Y. Zhong, S. Li, A 3D shape design and optimization method for natural laminar flow nacelle, in: Proceedings of ASME Turbo Expo 2017: Turbomachinery Technical Conference and Exposition, Paper Number GT2017-64379, vol. 1, 2017, pp. 825–830.
[39] S. Kirkpatrick, C.D. Gelatt, M.P. Vecchi, Optimization by simulated annealing, Science 220 (4598) (1983) 671–680.
[40] F. Tejero, D. MacManus, C. Sheaf, Surrogate-based aerodynamic optimisation of compact nacelle aero-engines, Aerosp. Sci. Technol. 93 (2019) 105207.
[41] B. Kulfan, Recent extensions and applications of the 'CST' universal parametric geometry representation method, Aeronaut. J. 114 (1153) (2010) 157–176.
[42] R. Christie, A. Heidebrecht, D.G. MacManus, An automated approach to nacelle parameterisation using intuitive class shape transformation curves, J. Eng. Gas Turbines Power 139 (6) (2017) 062601.
[43] R. Christie, M. Robinson, F. Tejero, D. MacManus, The use of hybrid intuitive class shape transformation curves in aerodynamic design, Aerosp. Sci. Technol. 95 (2019) 105473.
[44] Ansys Inc., 275 Technology Drive, Canonsburg, PA 15317, ANSYS ICEM CFD Tutorial Manual.
[45] Ansys Inc., 275 Technology Drive, Canonsburg, PA 15317, ANSYS FLUENT User's Guide.
[46] F.R. Menter, Two-equation eddy-viscosity turbulence models for engineering applications, AIAA J. 32 (8) (1994) 1598–1605.
[47] W. Sutherland, The viscosity of gases and molecular force, Philos. Mag. 5 (35) (1893) 507–531.
[48] AGARDograph AG-237, Guide to In-Flight Thrust Measurement of Turbojets and Fan Engines, Tech. Rep., AGARD Report, 1979.
[49] M. Sierra, C.C.A. Coello Coello, Improving PSO-based multi-objective optimization using crowding, mutation and ϵ-dominance, in: Evolutionary Multi-Criterion Optimization, Springer, Berlin Heidelberg, 2005, pp. 505–519.
[50] J.T. Knight, D.J. Singer, M.D. Collette, Testing of a spreading mechanism to promote diversity in multi-objective particle swarm optimization, Optim. Eng. 16 (2015) 279–302.
[51] L. Li, J. Bai, T. Guo, X. He, Z. Fu, Aerodynamic design of the supersonic aircraft wing-shape and wing-twist optimization, Int. J. Aeronaut. Space Sci. 19 (2018) 340–353.
[52] F. Sanchez-Moreno, D. MacManus, F. Tejero, J. Matesanz-Garcia, C. Sheaf, Robustness of optimisation algorithms for transonic aerodynamic design, in: Proceedings of 9th European Conference for, in: Aeronautics and Space Sciences, vol. EUCASS-3AF, 2022.
[53] L. Pronzato, W.G. Muller, Design of computer experiments: space filling and beyond, Stat. Comput. 22 (3) (2012) 681–701.
[54] J.C. Helton, F.J. Davis, Latin hypercube sampling and the propagation of uncertainty in analyses of complex systems, Eng. Syst. Saf. 81 (2003) 23–69.
[55] H. Jiangtao, G. Zhenghong, Z. Zhu, Z. Ke, An improved adaptive sampling and experiment design method for aerodynamic optimization, Chin. J. Aeronaut. 28 (5) (2015) 1391–1399.
[56] S. Shanmuganathan, S. Samarasinghe, Artificial Neural Network Modelling, Springer International Publishing, 2016.
[57] V.J. Mawson, B.R. Hughes, Coupling simulation with artificial neural networks for the optimisation of HVAC controls in manufacturing environments, Optim. Eng. 22 (2021) 103–119.
[58] S. Haykin, Neural Networks and Learning Machines, Pearson, 2008.
[59] K. Santosh, N. Das, S. Ghosh, Deep learning: a review, in: Deep Learning Models for Medical Imaging: Primers in Biomedical Imaging Devices and Systems, 2022, pp. 29–63.
[60] I. Goodfellow, Y. Bengio, A. Courville, Deep Learning, The MIT Press, 2016, Illustrated edition.
[61] M. Lau, K. Lim, Review of adaptive activation function in deep neural network, in: Conference on Biomedical Engineering and Sciences, 2018.
[62] A.H.A.L. Maas, A. Ng, Rectifier nonlinearities improve neural network acostic models, in: International Conference on Machine Learning, Atlanta, Georgia, USA, 2013.
[63] S. Haykin, Neural Networks: A Comprehensive Foundation, Prentice Hall PTR, 1998.
[64] M. Buscema, Back propagation neural networks, Subst. Use Misuse 33 (2) (1988) 233–270.
[65] D. Kingma, J. Ba, ADAM: a method for stochastic optimization, in: 3rd International Conference on Learning Representation, 2015.
[66] X. Ying, An overview of overfitting and its solutions, J. Phys. Conf. Ser. 1168 (2019) 022022.
[67] F. Tejero, D. MacManus, J. Matesanz-Garcia, A. Swarthout, C. Sheaf, Towards the design and optimisation of future compact aero-engines: intake/fancowl trade-off investigation, Int. J. Numer. Methods Heat Fluid Flow (2022).
[68] A. Benaouali, S. Kachel, Multidisciplinary design optimization of aircraft wing using commercial software integration, Aerosp. Sci. Technol. 92 (2019) 766–776.

2023-03-03

Neural network-based multi-point, multi-objective optimisation for transonic applicatio

Tejero, Fernando

Elsevier

Tejero F, MacManus DG, Sanchez-Moreno F, Sheaf C. (2023) Neural network-based multi-point, multi-objective optimisation for transonic applications. Aerospace Science and Technology, Volume 136, May 2023, Article number 108208

https://doi.org/10.1016/j.ast.2023.108208